This is a repository copy of *Damage tolerance and toughness of elderly human femora*.

White Rose Research Online URL for this paper:
http://eprints.whiterose.ac.uk/172404/

Version: Published Version

Article:

Martelli, S., Giorgi, M., Dall' Ara, E. et al. (1 more author) (2021) Damage tolerance and toughness of elderly human femora. Acta Biomaterialia, 123. pp. 167-177. ISSN 1742-7061

https://doi.org/10.1016/j.actbio.2021.01.011

Reuse

This article is distributed under the terms of the Creative Commons Attribution-NonCommercial-NoDerivs (CC BY-NC-ND) licence. This licence only allows you to download this work and share it with others as long as you credit the authors, but you can't change the article in any way or use it commercially. More information and the full terms of the licence here: https://creativecommons.org/licenses/

Takedown

If you consider content in White Rose Research Online to be in breach of UK law, please notify us by emailing eprints@whiterose.ac.uk including the URL of the record and the reason for the withdrawal request.

eprints@whiterose.ac.uk
https://eprints.whiterose.ac.uk/

Acta Biomaterialia 123 (2021) 167–177

Contents lists available at ScienceDirect

Acta Biomaterialia

journal homepage: www.elsevier.com/locate/actbio

Full length article

Damage tolerance and toughness of elderly human femora

Saulo Martelli[a,b,*], Mario Giorgi[c,d], Enrico Dall' Ara[c], Egon Perilli[b]

[a] School of Mechanical, Medical and Process Engineering, Queensland University of Technology, Brisbane, Australia
[b] Medical Device Research Institute, College of Science and Engineering, Flinders University, Adelaide SA, Australia
[c] Department of Oncology and Metabolism and Insigneo Institute for in Silico Medicine, University of Sheffield, Sheffield, UK
[d] Certara QSP, Certara UK Limited, Level 2-Acero, 1 Concourse Way, Sheffield, S1 2BJ, UK

ARTICLE INFO

Article history:
Received 27 October 2020
Revised 22 December 2020
Accepted 9 January 2021
Available online 14 January 2021

Keywords:
Bone fracture prevention
Fracture risk assessment
Osteoporosis
Biomechanics
Elastic instability

ABSTRACT

Observations of elastic instability of trabecular bone cores supported the analysis of cortical thickness for predicting bone fragility of the hip in people over 60 years of age. Here, we falsified the hypothesis that elastic instability causes minimal energy fracture by analyzing, with a micrometric resolution, the deformation and fracture behavior of entire femora. Femur specimens were obtained from elderly women aged between 66 – 80 years. Microstructural images of the proximal femur were obtained under 3 – 5 progressively increased loading steps and after fracture. Bone displacements, strain, load bearing and energy absorption capacity were analyzed. Elastic instability of the cortex appeared at early loading stages in regions of peak compression. No elastic instability of trabecular bone was observed. The subchondral bone displayed local crushing in compression at early loading steps and progressed to 8 – 16% compression before fracture. The energy absorption capacity was proportional to the displacement. Stiffness decreased to near-zero values before fracture. Three-fourth of the fracture energy (10.2 – 20.2 J) was dissipated in the final 25% force increment. Fracture occurred in regions of peak tension and shear, adjacent to the location of peak compression, appearing immediately before fracture. Minimal permanent deformation was visible along the fracture surface. Elastic instability modulates the interaction between cortical and trabecular bone promoting an elastically stable fracture behavior of the femur organ, load bearing capacity, toughness, and damage tolerance. These findings will advance current methods for predicting hip fragility.

Statement of significance

Bone elastic instability has been observed in trabecular bone cores and thought to determine the steep increase of the risk of hip fractures in the elderly population. Here, we analyzed the microstructural deformation and fracture behavior of entire elderly femora. Elastic instability of the cortex promoted crushing of the subchondral bone, which reached compression levels (8–16%) unseen before in trabecular bone cores. The deformation energy was a monotonic rising function of compression as stiffness decreased to near-zero values before fracture. Therefore, cortical elastic instability promotes, rather than disrupt, load bearing capacity, toughness, and damage tolerance in the most vulnerable people. These findings will advance current bone fracture mechanics discipline and impact to the prediction and prevention of fragility fractures.

© 2021 Acta Materialia Inc. Published by Elsevier Ltd.
This is an open access article under the CC BY-NC-ND license
(http://creativecommons.org/licenses/by-nc-nd/4.0/)

1. Introduction

The remarkable combination of light weight, high strength and toughness of bone, three generally mutually exclusive properties, has inspired the development of new engineering structures [1], biomimetic materials and systems [2,3], and has enabled studying anatomical similarities between animal species [4], inferring on

---

[*] Corresponding author at: School of Mechanical, Medical and Process Engineering, Queensland University of Technology, Brisbane, Australia.
E-mail address: saulo.martelli@qut.edu.au (S. Martelli).

https://doi.org/10.1016/j.actbio.2021.01.011
1742-7061/© 2021 Acta Materialia Inc. Published by Elsevier Ltd. This is an open access article under the CC BY-NC-ND license (http://creativecommons.org/licenses/by-nc-nd/4.0/)

hominid's lifestyle [5], evaluating stability of orthopedic implants [6] and managing age-related bone health complications [7,8]. Yet, elastic instability is thought to cause the steeply exponential increase of hip fractures in the population over 60 years of age, in apparent contrast with the notion that bone architecture adapts to best support loading across the entire lifespan [7,9].

Bone fracture is determined by several toughening mechanisms occurring at different length scales. Past yield, isolated lamellae display ductile behavior, no damage [10], whereas compact osteonal bone displays progressive accumulation and coalescence of fine cracks at lamellar interfaces and in correspondence of bone pores [10]. Isolated fibril bridging, ligament bridging, and crack deflection are toughening mechanisms in bone tissue. However, a variety of failure modes like elastic instability, barreling, rotation and band-like failure have been observed at a larger length-scale in 5 – 10 mm trabecular bone cores [9,11], hence suggesting a variable failure behavior in entire femur organs. Yet, observing elastic instability in entire femur organs has been prohibitively challenging due to the difficulty of measuring cortical and trabecular displacements under load over the entire femur volume.

There have been of course several studies investigating the failure of entire human femora providing, at times, controversial conclusions. Fracture of the hip in elderly individuals with low cortical and trabecular thickness has been attributed to elastic instability from calculations of critical stress [7] and measurements of trabecular displacements in isolated bone cores compressed to fracture [9]. In apparent contrast, continuum mechanics models assuming no elastic instability showed high precision ($R^2 = 0.80$ – 0.97) in predicting cortical strain, femoral strength and fracture pattern in donors of 46 – 96 years of age [12–14], otherwise suggesting elastic stability of human femora over the entire life span. Furthermore, continuum models using bone elastic properties obtained by testing isolated bone cores, systematically underestimated by 21 – 29 % femoral strength under habitual loading configurations [12,13,15,16], suggesting that failure behavior in isolated bone cores may differ from that in whole femur organs. For example, it is possible that the confinement provided by the cortex modulates damage onset and progression in whole femur organs, preventing elastic instability and promoting support and damage tolerance [17]. The recent advance of large-object time-lapsed micro-Computed-Tomography (μCT) has enabled imaging the microstructure of entire bone organs under load [18]. Here, we analyze microstructural images of the proximal half of elderly human femora loaded to fracture to falsify the hypothesis that elastic instability causes minimal energy failure in the elderly population.

We ask the following questions: How does the human femur deform? How does damage and energy dissipation initiate and progress to complete failure? What is the failure mechanism and energy absorption capacity in femur organs? To answer these questions, we analyzed time-elapsed microstructural images of the proximal half of the excised femur of four elderly women, which were expected to show elastic instability. Elastic instability was assessed by examining cortical and trabecular displacements in the image sequences before fracture in relation to the reaction force profile, such that if elastic instability occurs, the reaction force is expected to drop, as displacements continue to increase before fracture. Energy dissipation was analyzed by comparing the images of the femur before loading and after fracture. Damage onset and progression was analyzed using bone strain calculations obtained via Digital Volume Correlation (DVC). Fracture onset was related to local strain values immediately before fracture. Femur stiffness and elastic energy were calculated using the loading sequence and the corresponding displacement in the images. The study was approved by the Social and Behavioral Ethics Committee of Flinders University (Project # 6380).

2. Materials and methods

The four donors were Caucasian women (66 – 80 years of age) with no reported history of fragility fracture. Specimens and a densitometry calibration phantom (Mindways Software, Inc., Austin, USA) with five dipotassium hydrogen phosphate samples (equivalent density range: 58.88 – 157.13 mg × cm-3) were imaged using a clinical CT scanner (Optima CT660, General Electric Medical Systems Co., Wisconsin, USA). The CT images were calibrated to equivalent bone mineral density levels in the phantom and projected on the quasi-frontal plane. The bone mineral content was obtained by integrating the bone mineral density over the total hip volume and divided by the hip area to provide the areal bone mineral density. A DXA-equivalent T-score level was calculated using the regression equation reported by Khoo and co-workers [19].

The images and the load profiles were obtained at the Australian Synchrotron (Clayton VIC, Australia) using a recent and yet unique large-object time-elapsed μCT protocol described earlier [18] (Fig. 1). In summary, the force increment was calculated for each specimen via a finite-element analysis of the clinical CT images. The specimen was potted distally 50 mm deep using dental cement. The hip load was applied to the specimen through a spherically shaped polyethylene pressure socket mimicking shape and stiffness of the natural acetabulum. The hip force orientation (8° hip abduction) represented a static single-leg stance task measured in total hip replacement patients wearing an instrumented hip implant [20]. A constant displacement was applied and progressively increased up to cause fracture of each specimen. Concomitant synchrotron-light μCT images of the microstructure of the proximal half of the femur (FOV: 4888 × 4888 × 4446 pixels, corresponding to 145.71 × 145.71 × 131.43 mm, isotropic pixel size: 0.03 mm) were obtained before loading, under 3 – 5 intermediate displacements and after fracture. The reaction force at the distal specimen was continuously recorded.

The Digital Volume Correlation algorithm developed at the University of Sheffield (BoneDVC, https://bonedvc.insigneo.org/dvc/) [21] was used to evaluate the strain distribution in the entire proximal femur under loading. Repeated images for two additional femoral heads (female, 68 years, 0.7 T-score and male, 72 years, -2 T-score) were obtained using the same imaging protocol used for the specimens, hence providing a zero-strain target for DVC calibration [21]. The relationship between strain error and grid size was determined for both the full resolution images (pixel size: 0.03 mm) and subsampled images (pixel size: 0.12 mm). Twelve (original resolution) and thirteen (subsampled images) isotropic grids were obtained for each image volume by varying the nodal spacing (spatial resolution of the DVC) from 10 voxels to 100 voxels using 10 voxels uniform steps. The nodal displacement was calculated by solving the registration equations in each node and using tri-linear interpolation within each grid-cell. The Cauchy's infinitesimal strain tensor was calculated for each grid using ANSYS (Ansys Inc, Canonsburg, USA) [22]. For each grid-size, the standard deviation of the error (SDER) was the average standard deviation of the six strain components across all the nodes of the grid. A power function was fitted to SDER and grid size (Supplementary figure S1) [23].

The strain analysis of the proximal half of the femur was performed using the subsampled images (pixel size: 0.12 mm), thereby providing information on the high strain regions object of the following full resolution analysis. The images were rigidly co-registered in space to the distal part of the femoral diaphysis in the intact specimen before loading (DataViewer, SkyScan–Bruker, Kontich, Belgium). The nodal spacing was set to 50 voxels, hence providing an isotropic grid size equal to 6 mm, which showed 0.076 % strain error in the calibration analysis. The volume outside of the specimen was excluded from the analysis to avoid artefacts, which

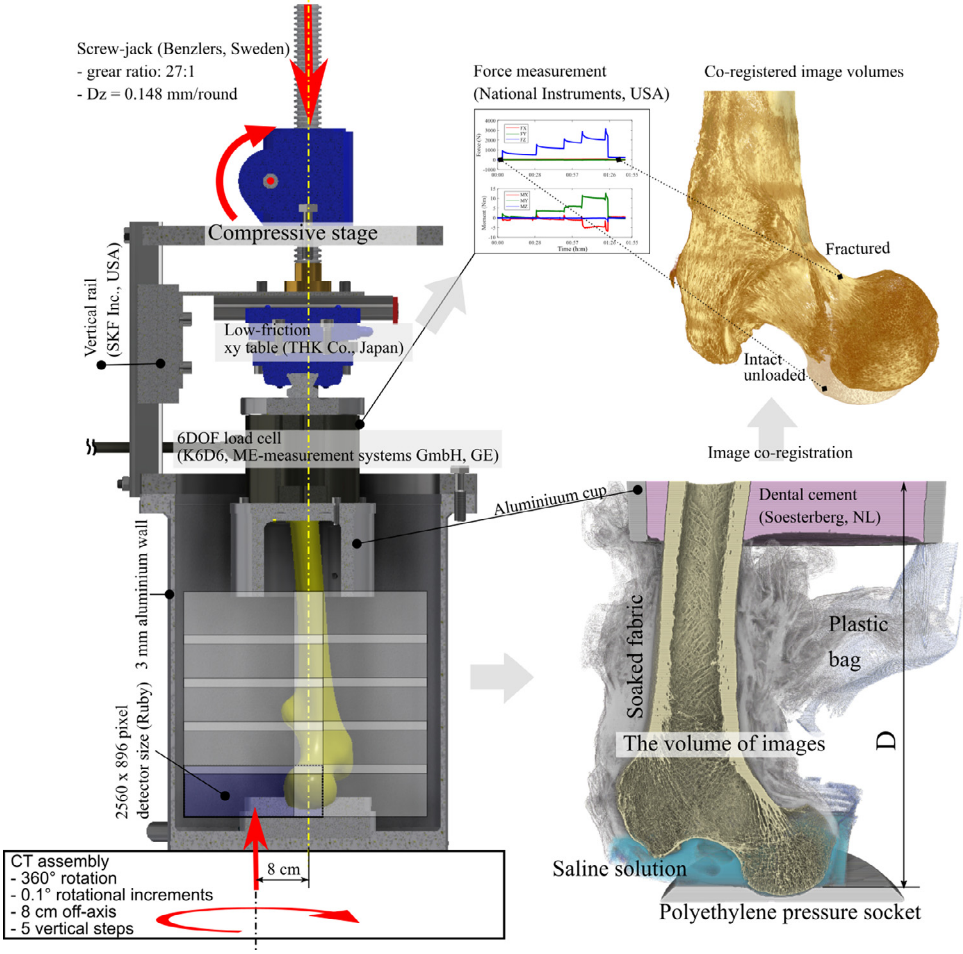

Fig. 1. The time-elapsed imaging protocol. The compressive stage, mounted on the CT assembly (Australian Synchrotron, Clayton VIC, Australia) is displayed on the left. In the top right, the images of one representative specimen before loading and after fracture are displayed co-registered in space. In the bottom left, the specimen mounted in the compression chamber. The pixels in the image were color-labeled and visualized showing the specimen (in light brown color), the pressure socket (grey), the saline solution (blue), the fabric wrapping around the specimen (grey), the plastic bag containing the saline solution (grey), and the distal aluminium cup (grey) potted with dental cement (pink). (For interpretation of the references to color in this figure legend, the reader is referred to the web version of this article.)

may be attributable to movements of the fabric, soaked in saline solution, wrapping the specimen for maintaining the bone moisture throughout the experiment. The analysis took approximately 7.5 h per load step on the HPC (ShARC, Dell PowerEdge C6320, 256GB RAM).

The femoral head and medial neck region, showing the highest strain levels in the analysis of the entire specimen, was studied in the full resolution images (pixel size: 0.03 mm). The images were rigidly co-registered in space to the images of the intact specimen before loading using as target a transversal slice at the height of the lesser trochanter (DataViewer, SkyScan–Bruker, Kontich, Belgium). The distal portion of the image volume was discarded. The strain analysis was conducted in two sub-volumes occupying up to 2 GB disk space (8-bit images) to meet the memory requirements of the BoneDVC algorithm [21]. The two volumes overlapped by no less than 100 voxels to account for border artefacts. The nodal spacing was set to 50 voxels providing an isotropic grid size equal to 1.5 mm, which showed 0.1 % strain error in the calibration analysis. The load step before fracture was analyzed for each specimen and took 22 h on an HPC machine (Dell PowerEdge C6320, RAM: 256GB).

The force and the displacement acting on the specimen were analyzed. The vertical position of the pressure socket was measured in the co-registered subsampled images by averaging the coordinates of three points manually identified on the distal surface of the pressure socket and adjacent to the femoral head contact area using Fiji [24]. The displacement was calculated using as reference the initial position of the socket. For specimen #1, the initial position was corrected by closing the initial gap between the femoral head and the socket. The peak vertical force at the time of load step application (F_0) and 30 minutes after (F_{30}) were analyzed. The peak deformation energy at load step application (E_0) and 30 minutes after (E_{30}) were calculated. Displacement, energy, and force at load step application were normalized to corresponding peak values in each specimen.

2.1. Data and statistical analysis

Specimens were classified as normal, osteopenic and osteoporotic according to the WHO guidelines using the calculated bone mineral density and T-score. Fracture patterns were classified according to common clinical fractures classification [25,26].

The displacements, strain and post-fracture inelastic deformation were analyzed in the subsampled images of the entire specimen and the respective DVC analysis. Strain maps calculated over the DVC grid where mapped to the images using cubic interpolation (Matlab, The MathWorks Inc., Natick, USA). A custom Matlab (The MathWorks, Natick, USA) routine was used to visualize the images, the displacement and strain maps superimposed. The elastic and inelastic deformation of the specimen was analyzed by overlaying the images of the specimen before loading, at the last load step before fracture and after fracture using Fiji [24]. For the

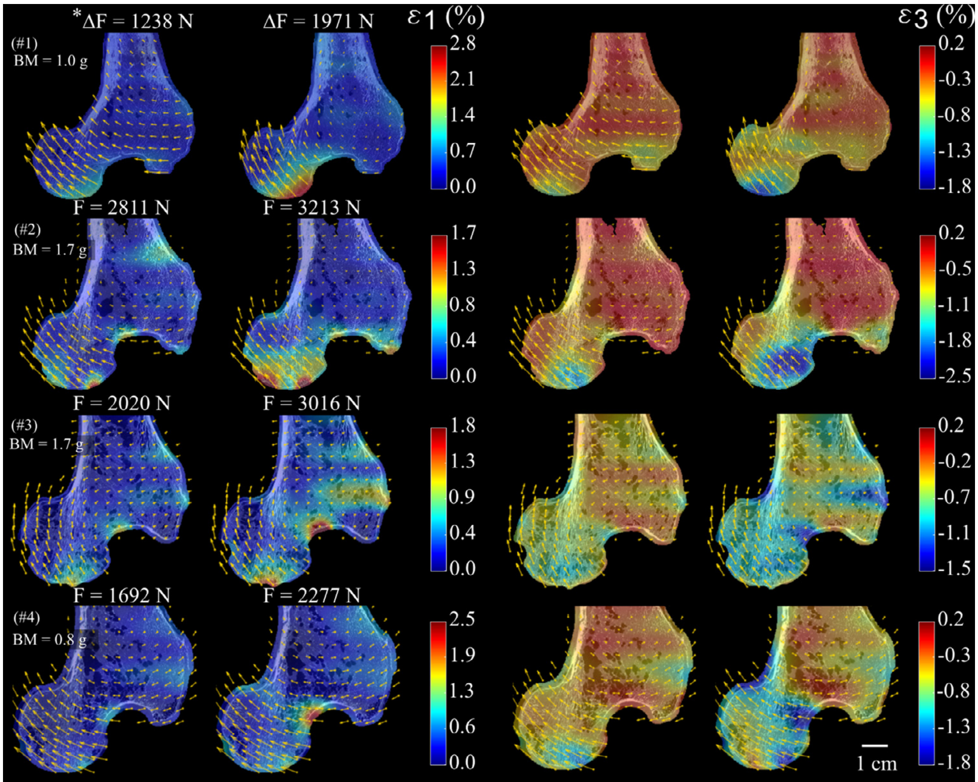

(*) the images for specimen #1 were registered to the images of the specimen subjected to 904 N (load step 1) because of movement artefacts in the greater trochanter region in the images of the specimen imaged before loading (load step 0, Table 1)

Fig. 2. The principal tensile and compressive strain maps ($\varepsilon 1$, $\varepsilon 3$) for the entire specimen (four femurs, one per row) calculated over bone cubes of 6 mm side length (pixel size = 0.12 mm, down sampled from 0.030 mm) for a mid-stage loading step and the last load step immediately before fracture. The maps display the proximal part of the specimen experiencing the highest strain levels in the entire specimen. The displacement vectors (yellow arrows) and the compressive force are also displayed, and the bone mass (BM) is reported for each specimen. (For interpretation of the references to color in this figure legend, the reader is referred to the web version of this article.)

fractured fragment, a second co-registration of the images was performed using as target a portion of the fragment away from the fracture surface and the superior head.

The progression of damage in the femoral head was analyzed in the full resolution images and the respective DVC analysis. Strain maps calculated over the DVC grid where mapped to the microstructural images using cubic interpolation, analyzed and visualized using Matlab© (The MathWorks Inc., Natick, USA), Dristhi [27], ImageJ (National Institute of Health, USA) and ParaView (Kitware, Clifton Park, NY, USA) for large volume visualization and animation.

The failure mode was analyzed in the full resolution images and the relative DVC analysis by comparing the images for the last frame before fracture to those of the fractured specimen.

The load support and energy absorption capacity were analyzed using force and displacement applied to the specimen. The deformation energy and the specimen stiffness were calculated. Force, displacement, and energy were analyzed using descriptive statistics. Force, displacement, and energy were normalized by the respective peak values to reduce inter-specimen variability. The association between normalized force, displacement, and deformation energy was studied using regression analysis. Statistical significance was set to $\alpha = 0.05$.

3. Results

3.1. Specimens classification

The bone mineral density range across the four specimens was 0.42–0.56 g/cm^2 thereby spanning by more than two standard deviations (T-score range = -2.09 – -4.75) the lower end of bone mineral density in the elderly population.

3.2. Whole femur strain and post-fracture inelastic deformation

Loading of the specimen caused the femoral head to rotate about the proximal shaft, moving medially in a quasi-frontal plane. Specimens showed either incomplete fracture, opening in the superior neck cortex or sub-capital shear failure, consistently with clinical fracture classifications [25,26]. The peak principal compressive strain calculated over cubic volumes of 6 mm side exceeded the 0.2% offset yield strain (0.7 – 1.2 %) in the superior femoral head and in the sub-capital neck, as the applied compression force exceeded the 50% of specimen strength. Focal tensile strain appeared just before fracture in, or adjacent to, regions of peak compression, reaching 1.7 – 2.8% (Fig. 2). Post-fracture residual displacement was mostly present in the superior femoral head at the location of peak compression while a marginal permanent deformation was observed along the fracture region. No residual displacement was apparent in the images over the remaining volume of the femur (Fig. 3).

3.3. Damage progression

The strain distribution in the femoral head and neck regions, calculated over a refined grid of cubic volumes of 1.5 mm side, showed compressive strain reaching 8 – 16% before fracture in localized in regions of a few millimeters in size (meso-scale) of peak compression (Fig. 4). The microstructural images displayed a progressive change in shape of the otherwise spherical head, showing flattening of the superior head over a circular area 17 – 24 mm

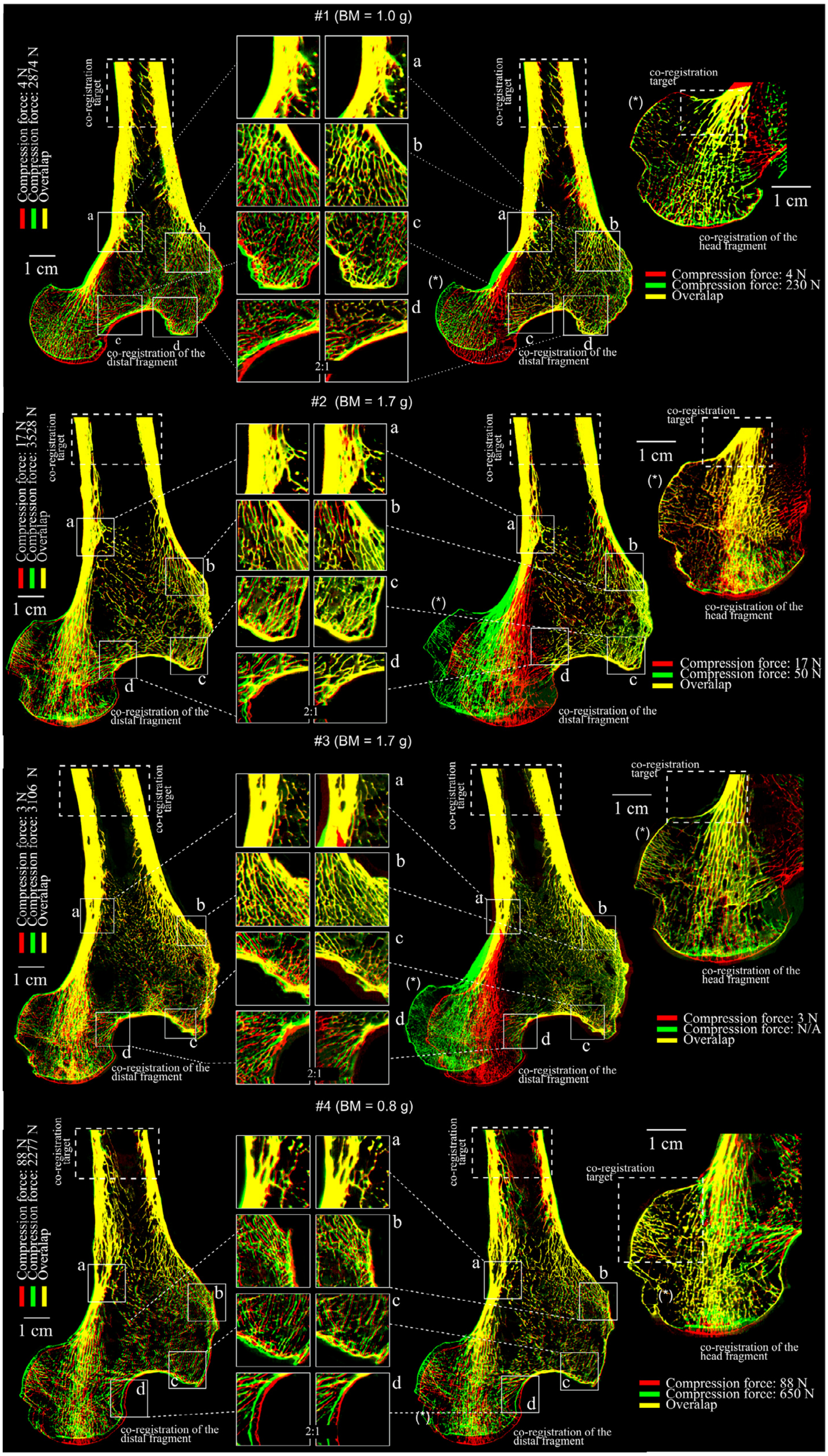

Fig. 3. The elastic and inelastic displacement. The images (pixel size = 0.12 mm, down sampled from 0.030 mm) of the specimen before loading (red) are overlaid to those of the specimen under load immediately before fracture (green, left) and after fracture (green, right). Overlapped regions are displayed in yellow. Details for trabecular structures in the calcar region (a), lateral greater trochanter (b), most proximal grater trochanter (c) and superior sub-capital neck (d) are displayed scaled up by factor 2. (For interpretation of the references to color in this figure legend, the reader is referred to the web version of this article.)

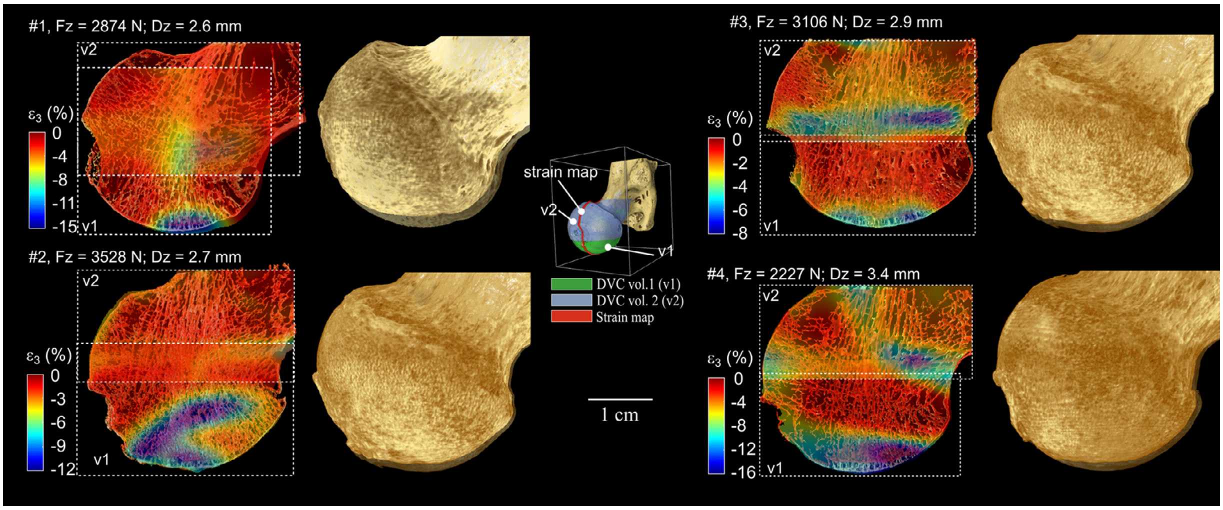

Fig. 4. The compressive strain map calculated over bone cubes of 1.5 mm side length (pixel size = 0.03 mm) in the femoral head and sub-capital neck immediately before fracture. On the right, the surface of the specimen before loading and under load are superimposed showing the change in geometry of each specimen.

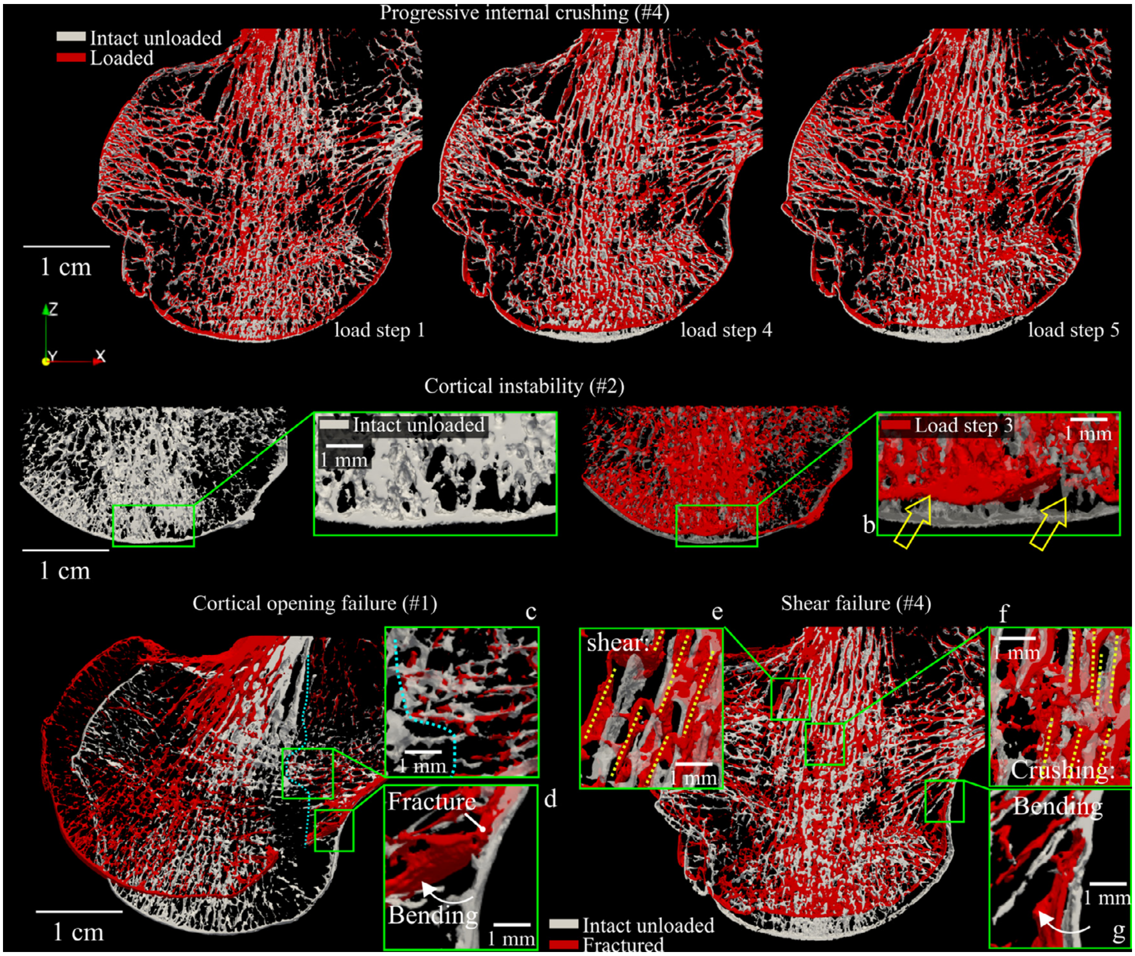

Fig. 5. The microstructural deformation in selected representative cases (unloaded specimen in grey color, loaded specimen in red). The progressive densification of the subchondral bone underneath the superior femoral head cortex is displayed (top row) for specimen #4 under load step 1, 4 and the last load step before failure (load step 5). The microarchitecture of the entire femoral head and sub-capital neck display no evidence of trabecular bending (top row). In the middle row, elastic instability of the superior head cortex occurs in correspondence of subcortical voids (a, b). In the bottom row, the bone microstructure before loading and after fracture in one representative case for cortical opening (specimen #1) and shear (specimen #4). Details along the fracture surface (blue dash line) are also displayed scaled by a convenient factor showing residual bending of the cortex after fracture (d, g), shear failure (e) and crushing (f) of the trabecular network and no permanent deformation of the trabecular network except in very close proximity of the fracture surface (c, d, e, f, g). (For interpretation of the references to color in this figure legend, the reader is referred to the web version of this article.)

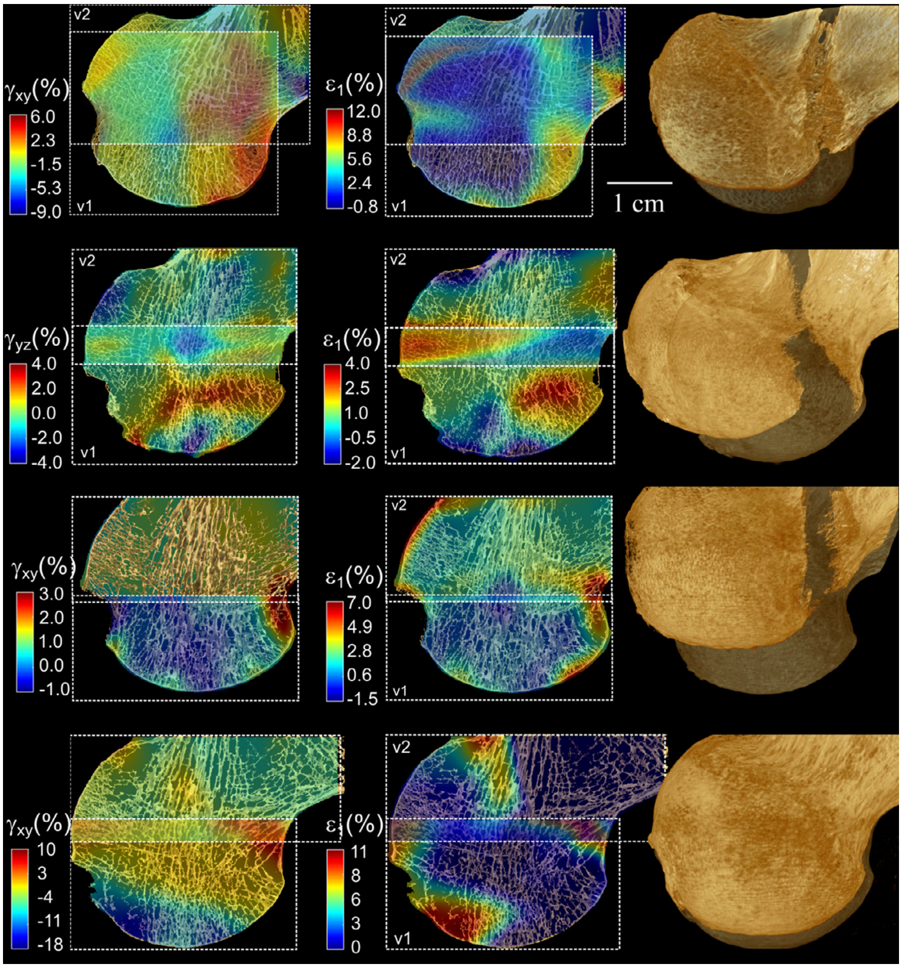

Fig. 6. The maps of the principal tensile and the shear strain component best representing the fracture location calculated immediately before fracture are displayed superimposed to the microstructural images of the intact unloaded specimen (left) (four femurs, one per row). On the right, the surface of the intact specimen before loading and after fracture are superimposed for reference with the corresponding strain maps displayed on the left. (For interpretation of the references to color in this figure legend, the reader is referred to the web version of this article.).

in diameter (area: 2.3–4.5 cm^2), which persisted after fracture (inelastic deformation) (Supplementary figure S2). The peak compressive strain was localized under the superior femoral head surface, showing bone densification via localized collapse of bone trabeculae best visible in the supplementary animations provided (Animations 2 – 5), and eventually progressed at increased loads to separate deeper regions of the femoral head volume (Supplementary figure S3). Within the flattened head surface area, the cortical shell showed localized bending toward the inner head accompanied by bone densification visible in the subchondral bone layer underneath the cortex. At no stage of the loading sequence there was a visible sign of trabecular elastic instability (Fig. 5).

3.4. Failure mode

Fracture onset occurred in regions adjacent to the flattened head surface, showing increased curvature of the bone surface. Fracture occurred by opening (specimen #1, #2 and #3) and shear (specimen #4) of the superior sub-capital head-neck junction (Fig. 5). For the cortical opening cases, the microstructural images displayed the fracture pattern running at normal angles through the main tensile trabecular group and the superior neck cortex, and then progressing further distally along the principal direction of the main compressive trabecular group, ending in the calcar region. A much-localized inelastic bending and fracture of the superior thin cortex was also visible. However, there was no visible inelastic deformation of the trabecular network over the whole fracture surface (Fig. 4). For the shear fracture case (specimen #4), shear failure of single trabeculae occurred along the shear plane at about 45° from the main direction of the principal compressive trabecular network. Concomitantly, the superior cortex rotated medially, fracturing by bending, and moving medially with the superior bone fragment. For all the four specimens, failure occurred under a complex deformation varying along all the six deformation axes. Opening of the superior cortex occurred under a combination of peak tensile (4 – 8%) and shear (3 – 6%) strain in regions of increased surface curvature while shear failure occurred under a combination of peak tensile (6 – 8%) and shear (3 – 10%) strain and high compression (8 – 12%) (Fig. 6). Cortical opening caused the load bearing capacity of the specimen to drop from 3546 ± 409 N to less than 220 N while the load bearing capacity in the shear failure case dropped from 2331 N to 661 N, showing the highest residual load bearing capacity among the specimens analyzed (Table 1).

3.5. Load support and energy absorption capacity

The displacement to fracture was less variable (4.4 – 5.0 mm; CV = 7%) than the failure load (2331 – 3965 N; CV = 21%) and the fracture energy (10.2 – 20.2 J; CV = 27%). The compressive force dropped to 61 ± 20% of the load step increase after 30 min (Fig. 7$_a$ and Table 1). The normalized total deformation energy stored in

Table 1
The time-elapsed compression experiment.

ID	D [mm]	ΔD [mm]	ΔD [%]	F_0 [N]	ΔF_0 [N]	ΔF_0 [%]	F_{30} [N]	ΔF_{30} [N]	ΔF_{30} [%]	K_0 [N/mm]	K_{30} [N/mm]	E_0 [J]	ΔE_0 [J]	ΔE_0 [%]	E_{30} [J]	ΔE_{30} [J]	ΔE_{30} [%]
1	0.00	-	-	-4	-	-	-	-	-	-	-	0.0	-	-	-	-	-
	0.40	0.40a)	8	904	904	29	490	490	46	2259	1225	0.4	0.4	2	0.2	0.2	46
	0.83	0.43	9	1557	654	21	1146	656	0.39	1527	1533	1.3	0.9	6	0.9	0.8	0.31
	1.67	0.84	17	2141	584	19	1718	572	43	692	678	3.6	2.3	15	2.9	1.9	27
	2.64	0.97	19	2874	733	23	2016	298	0.74	755	307	7.6	4.0	26	5.3	2.5	0.48
	4.99	2.35	47	3146	272	9	220	-1796	-	116	-	15.7	8.1	52	-	-	-
2	0.00	-	-	13	-	-	-	-	-	-	-	0.0	-	-	-	-	-
	0.73	0.73	15	1514	1514	43	684	684		2078	939	1.1	1.1	7	0.5	-	-
	1.43	0.71	14	2176	662	19	1453	769	0.48	938	1090	3.1	2.0	13	2.1	1.6	0.40
	1.88	0.45	9	2811	635	18	2134	681	50	1408	1510	5.3	2.2	14	4.0	1.9	40
	2.66	0.77	16	3528	717	20	1993	822	1.10	925	1061	9.4	4.1	26	5.3	1.3	0.76
	4.94	2.28	46	3213	-315	-9	51	-	-	-138	-	15.9	6.5	41	-	-	-
3	0.00	-	-	3	-	-	-	-	-	-	-	0.0	-	-	-	-	-
	1.08	1.08	21	1000b)	1000	25	-	-	-	930	-	1.1	1.1	5	-	-	-
	1.82	0.74	15	2020	1020	26	921	-	-	1378	-	3.7	2.6	13	1.7	-	-
	2.89	1.08	21	3106	1086	27	2019	1098	50	1010	1021	9.0	5.3	26	5.8	4.2	43
	5.09	2.20	43	3965	859	22	-	-	-	391	-	20.2	11.2	55	-	-	-
4	0.00	-	-	86	-	-		-	-	-	-	0.0	-	-	-	-	-
	0.66	0.66	15	919	919	39	446	-	-	1394	-	0.6	0.6	6	0.3	-	-
	1.27	0.61	14	1409	490	21	766	320	67	800	522	1.8	1.2	12	1.0	0.7	55
	2.05	0.77	18	1692	283	12	985	219	0.76	365	283	3.5	1.7	16	2.0	1.0	0.58
	2.66	0.61	14	1982	290	12	1254	269	73	473	439	5.3	1.8	18	3.3	1.3	59
	3.35	0.69	16	2277	295	13	1639	385	0.62	425	555	7.6	2.4	23	5.5	2.2	0.50
	4.36	1.01	23	2331	54	2	661	-	-	54	-	10.2	2.5	25	-	-	-

Abbreviations

D Displacement in millimeters.

ΔD Displacement step increment in mm and % of peak D.

F_0 Force at time of load step application in Newton.

ΔF_0 Force step increment in Newtons and % of peak F_0.

F_{30} Force after 30' from load step application in Newton.

ΔF_{30} Force step increment after 30' from load step application in Newtons and % of peak F_0.

K_0 Stiffness at time of load step application (N/mm).

K_{30} Stiffness at 30' from load step application (N/mm).

E_0 Deformation energy at time of load step application in Joule.

ΔE_0 Deformation energy: step increment at load step application (Joule and % of peak energy E_0).

E_{30} Deformation energy at 30' from load step application in Joule.

ΔE_{30} Deformation energy: step increment 30' after load step application in Joule and % of peak energy E_0.

a) The displacement was corrected to account for the initial gap.

b) The load step was set to the nominal load step due to data loss.

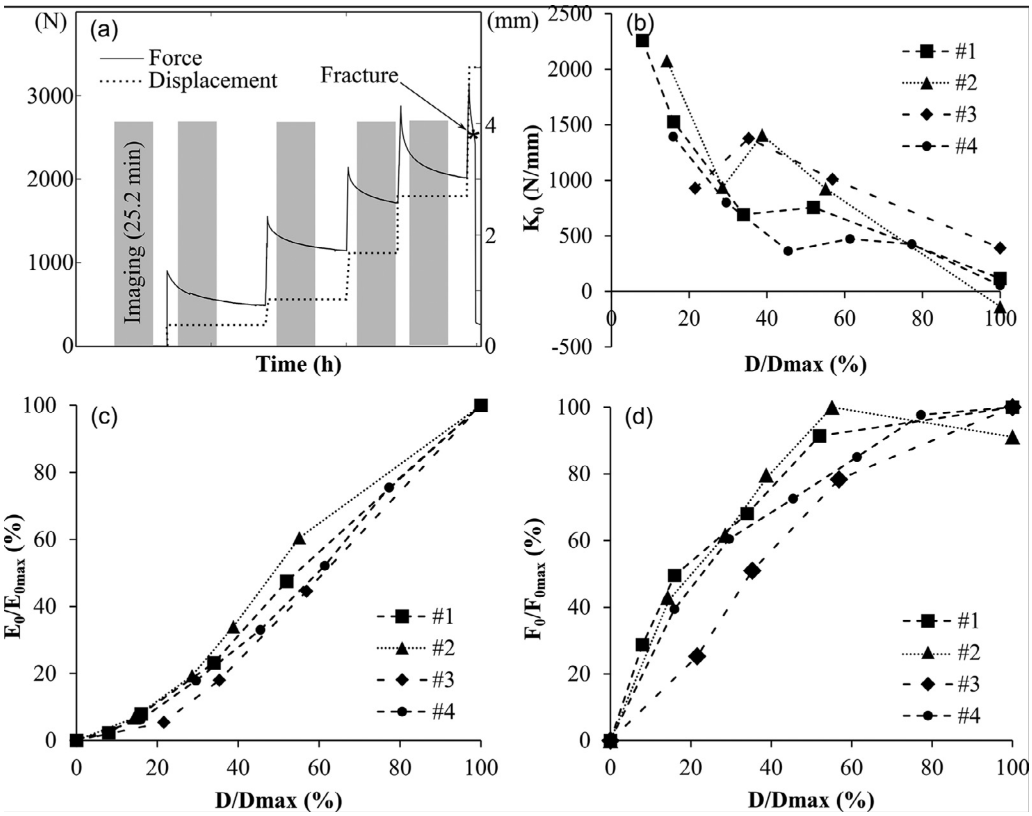

Fig. 7. Stiffness, force, and deformation energy response to controlled displacement. The figure displays a representative (specimen #1) force and displacement time history (a). The stiffness (K0) (b), the normalized deformation energy (E0/E0max) (c) and the normalized force at the time of load step application (F0/F0max) (d) are plotted against the normalized displacement (D/Dmax).

the specimen at the time of load step application was a linear function of the displacement (proportionality coefficient: 1.12 – 1.27, $R^2 = 0.97 – 0.99$, $p < 0.01$) for a normalized displacement greater than 20% (Fig. 7$_{c}$). The force monotonically increased up to fracture, showing a decrease in stiffness to near-zero value immediately before fracture; the 75% of fracture energy (10.2 – 20.2 J) was generated for the final 25% force increment (Fig. 7$_{b,d}$). The only exception was specimen #2, which showed an 8% decrement of the force as the last displacement step increase was applied; this occurred concomitantly with the collapse in compression of a separate large bone portion deeper in the femoral head (Supplementary figure 3).

4. Discussion

We analyzed the deformation and facture mechanism in four femur specimens spanning the lower end of bone quality in humans. We found that loading to fracture some of the most vulnerable femora did cause a highly localized elastic instability of their superior cortex, which enhanced, rather than disrupted, mechanical support, energy absorption capacity and damage tolerance of the femur organ, a property mainly provided by the elastic response of the trabecular bone. As such, by showing the distinct and complementary roles of cortical and trabecular bone, conjointly contributing to the toughness of femur organs at advanced age, these findings will inform the research into the unmet need of fracture prevention [28].

We observed cortical instability in bone regions under peak compression, which caused local stress relaxation of the cortex, and deformation of subchondral bone reaching a remarkably high 8 – 16 % strain predominantly in compression before fracture, thereby largely exceeding the ultimate strain reported earlier (up to 4%) for excised trabecular bone cores [9] and providing energy dissipation capacity (inelastic strain) by crushing in compression of the subchondral bone (Figs. 2–4). We also observed that the force was a monotonic rising function of displacement and that the total (elastic and inelastic) deformation energy was proportionally increasing as displacement increased up to fracture (Fig. 7). Hence, cortical instability promotes, rather than disrupts, mechanical support and toughness in some of the weakest human femora, likely by modulating the confinement of the subchondral bone under the highest compression. This finding demonstrates cortical and trabecular synergies determining the femur's deformation response to loading, which modulates the femur's damage tolerance capacity largely provided by the trabecular bone. Regarding femur's fracture behavior, fracture onset did not occur in regions of cortical instability, but rather in nearby regions of increased curvature appearing at late loading stages and under a complex three-dimensional deformation state showing peak tensile and shear strain. Fracture then propagated to complete fracture by dissipating minimal energy, as evidenced by the minimal inelastic strain along the entire fracture surface. Bending of the cortex was visible in the images of the fractured specimen but not in the images preceding fracture, hence suggesting no significant elastic instability of the cortex at the location of fracture onset. Therefore, it appears that bending is the dominant fracture behavior of the cortex caused by changes of cortical curvature at late loading stages resulting from the large deformation of the nearby region under the highest compression.

Earlier studies showed a variety of failure modes in excised trabecular bone cores (5–10 mm size), in contrast with the consistent failure behavior found in all the four entire proximal femurs analyzed here. Furthermore, isolated bone cores under compression showed elastic instability above 2% compression and reached 4% deformation before fracture [9]. In contrast, as shown here at the organ scale, femurs displayed no elastic instability, as evaluated from the images over the trabecular volume of the entire proximal femur, and a much higher deformation before fracture (8 – 16% compression). As such, the high post-yield deformation, indicating damage accumulation, and the progressive decrease of bone stiffness, provides the femur with enhanced energy absorption capacity, or toughness, and mechanical support as load increases. These findings are consistent with the ductile-to-brittle transition of cortical bone's inelastic behavior showing damage creation, stress redistribution, energy dissipation and damage localization leading to brittle failure [29]. However, the ultimate strain shown here in femur organs is about one order of magnitude higher than that observed in compact bone [29]. These findings indicate that 1) the spatial bone organization in the proximal femur provides bone with superior deformation capacity than that observed in isolated bone cores and; 2) elastic instability, often considered the epitome of engineering failure, is less likely to cause minimal energy fracture in femur organs than in isolated bone cores [7,9]. As such, these findings reconcile bone mechano-adaptation principles and fracture behavior in human femora.

It is important to note that in people, hip fractures mostly occur while falling on a side, which would cause the center of pressure of the hip to move medially, reversing the load in the superior neck from tension to compression with respect to what shown here, hence causing increased propensity for instability of the thin cortex in the superior neck [7]. However, current models that assume quasi-brittle fracture behavior and no elastic instability, did underpredict (rather than overpredict) by 9% the fracture load [12,13], otherwise suggesting a moderate effect of elastic instability also while falling on the side and a similar failure mechanism to that reported here. Here, we demonstrate the microstructural mechanism for support and damage tolerance under habitual loading, which represents a condition of maximal strength, as reflected by the co-location of the center of pressure and the high-density main compressive trabecular network (Fig. 4). Different motor tasks load different areas of the hip at different loading rates and rely on reduced trabecular support and load bearing capacity. This effect is emphasized during aging, as the amount and variety of physical activity reduces, and bone loss is more pronounced in the less loaded regions. In comparison, the fracture energy reported here for habitual loading (10.2–20.2 J) is more than twice that measured during a fall on the side (2–8 J) [30], while both scenarios similarly displayed deformation of the cortex to fracture well above yield and exceeding 3% [31,32]. These differences are consistent with the almost double femoral strength under habitual loading configurations [13] and the larger damage tolerance and post-yield deformation of bone at low strain rates [29]. Although higher loading rates can create more favorable conditions for the onset of elastic instability, the present results are directly comparable with earlier studies similarly using quasi-static loading [9,33] or exclusively geometrical considerations for supporting the theory of elastic instability [7]. Also, the fracture behavior shown here in four femora may not be generalized to bones from different anatomical sites, different loading conditions and may not represent femur's fracture behavior across the entire human population. Nevertheless, the importance of the present study is in showing specific, elastically stable, fracture behavior in some of the weakest femora, which were otherwise expected to show an early drop in energy absorption capacity caused by elastic instability, as theorized by early calculations of critical stress [7] and inferred from direct observations of trabecular bone cores [9]. As such, elastic instability appears no longer the only logical explanation for the steep exponential increase of hip fracture incidence in people above 60 years of age. The same elastically stable fracture behavior shown here, together with the loss of trabecular support in regions not subjected to habitual loading, can concur in explaining the higher propensity to fracture in older people and provides an alternative target for fragility prediction and preventive treatments.

5. Conclusion

For facture prediction, the interdependence between cortical and trabecular compartments shown here emphasizes the need to account for the contribution to mechanical support of both cortical and trabecular bone. For example, models accounting for bone distribution in the entire hip region using three-dimensional imaging methods appear better suited to predict fragility, than other methods focusing on local values of cortical thickness [7]. By showing enhanced deformation and support in human femur, the present findings can inform the advancement of current technologies for the fragility prediction. Preventative solutions may help understanding the causes and mitigate the burden of hip fracture. As aging typically leads to reduced bone mass particularly in bone regions subjected to infrequent (unusual) motor tasks, these observations may help explaining the beneficial effect of odd-impact activities on hip health [34], the decreased prevalence of hip fracture in societies with higher and more variable activity levels [7] and, as part of our society's drive for healthy ageing, exercise treatments to promote bone health [35]. For example, a new generation of anabolic treatments, alongside the traditional anti-resorptive treatments, may be able to specifically target femoral regions of most pronounced bone loss in frail people. These findings will inform testable interventions to mitigate the burden of hip fragility [7,8] and will continue to inspire related fields of engineering [1], material science [2,3], orthopedics [6] and human evolution [4,5].

Declaration of Competing Interest

Certara QSP provided the salary for MG during the writing of the manuscript but did not have any additional role in the study design, data collection and analysis, decision to publish, or preparation of the manuscript. All the other authors declare no conflict of interest in relation to the present study.

Acknowledgments

The Australian Research Council (DP180103146; FT180100338), the Australian Synchrotron (Clayton, VIC, Australia) and the Engineering and Physical Sciences Research Council (EP/K03877X/1; EP/S032940/1) are gratefully acknowledged.

Supplementary materials

Supplementary material associated with this article can be found, in the online version, at doi:10.1016/j.actbio.2021.01.011.

References

[1] J. Wu, N. Aage, R. Westermann, O. Sigmund, Infill optimization for additive manufacturing – approaching bone-like porous structures, IEEE Trans. Vis. Comput. Graph. (2017) 1–1, doi:10.1109/TVCG.2017.2655523.

[2] C. Sanchez, H. Arribart, M. Madeleine, G. Guille, Biomimetism and bioinspiration as tools for the design of innovative materials and systems, Nat. Mater. 4 (2005) 277–288, doi:10.1038/nmat1339.

[3] U.G.K. Wegst, H. Bai, E. Saiz, A.P. Tomsia, R.O. Ritchie, Bioinspired structural materials, Nat. Mater. 14 (2015) 23–36, doi:10.1038/nmat4089.

[4] C.T. Rubin, Skeletal strain and the functional significance of bone architecture, Calcif. Tissue Int. 36 (1984) 11–18, doi:10.1007/BF02406128.

[5] C.O. Lovejoy, Evolution of human walking, Sci. Am. 259 (1988) 118–125.

[6] J. Kerner, R. Huiskes, G.H. Van Lenthe, H. Weinans, B. Van Rietbergen, C.A. Engh, A.A. Amis, Correlation between pre-operative periprosthetic bone density and post-operative bone loss in THA can be explained by strain-adaptive remodelling, J. Biomech. 32 (1999) 695–703, doi:10.1016/S0021-9290(99)00041-X.

[7] P.M. Mayhew, C.D. Thomas, J.G. Clement, N. Loveridge, T.J. Beck, W. Bonfield, C.J. Burgoyne, J. Reeve, Relation between age, femoral neck cortical stability, and hip fracture risk, Lancet 366 (2005) 129–135, doi:10.1016/S0140-6736(05)66870-5.

[8] A. Heinonen, P. Kannus, H. Sievänen, P. Oja, M. Pasanen, M. Rinne, K. Uusi-Rasi, I. Vuori, Randomised controlled trial of effect of high-impact exercise on selected risk factors for osteoporotic fractures, Lancet 348 (1996) 1343–1347, doi:10.1016/S0140-6736(96)04214-6.

[9] A. Nazarian, M. Stauber, D. Zurakowski, B.D. Snyder, R. Müller, The interaction of microstructure and volume fraction in predicting failure in cancellous bone, Bone 39 (2006) 1196–1202, doi:10.1016/j.bone.2006.06.013.

[10] J. Schwiedrzik, R. Raghavan, A. Bürki, V. LeNader, U. Wolfram, J. Michler, P. Zysset, In situ micropillar compression reveals superior strength and ductility but an absence of damage in lamellar bone, Nat. Mater. 13 (2014) 740–747, doi:10.1038/nmat3959.

[11] E. Perilli, M. Baleani, C. Öhman, R. Fognani, F. Baruffaldi, M. Viceconti, Dependence of mechanical compressive strength on local variations in microarchitecture in cancellous bone of proximal human femur, J. Biomech. 41 (2008) 438–446, doi:10.1016/j.jbiomech.2007.08.003.

[12] E. Dall'ara, B. Luisier, R. Schmidt, F. Kainberger, P. Zysset, D. Pahr, A nonlinear QCT-based finite element model validation study for the human femur tested in two configurations in vitro, Bone 52 (2013) 27–38, doi:10.1016/j.bone.2012.09.006.

[13] E. Schileo, L. Balistreri, L. Grassi, L. Cristofolini, F. Taddei, T. Medica, I.O. Rizzoli, To what extent can linear finite element models of human femora predict failure under stance and fall loading configurations? J. Biomech. 47 (2014) 3531–3538, doi:10.1016/j.jbiomech.2014.08.024.

[14] E. Schileo, E. Dall'ara, F. Taddei, A. Malandrino, T. Schotkamp, M. Baleani, M. Viceconti, An accurate estimation of bone density improves the accuracy of subject-specific finite element models, J. Biomech. 41 (2008) 2483–2491, doi:10.1016/j.jbiomech.2008.05.017.

[15] L. Rincón-Kohli, P.K. Zysset, Multi-axial mechanical properties of human trabecular bone, Biomech. Model. Mechanobiol. 8 (2009) 195–208, doi:10.1007/s10237-008-0128-z.

[16] C. Falcinelli, E. Schileo, L. Balistreri, F. Baruffaldi, B. Bordini, M. Viceconti, U. Albisinni, F. Ceccarelli, L. Milandri, A. Toni, F. Taddei, Multiple loading conditions analysis can improve the association between finite element bone strength estimates and proximal femur fractures: a preliminary study in elderly women, Bone 67 (2014) 71–80, doi:10.1016/j.bone.2014.06.038.

[17] P. Podsiadlo, A.K. Kaushik, E.M. Arruda, A.M. Waas, B.S. Shim, J. Xu, H. Nandivada, B.G. Pumplin, J. Lahann, A. Ramamoorthy, N.A. Kotov, Ultrastrong and Stiff Layered Polymer Nanocomposites, Science 318 (2007) 80–83 80-., doi:10.1126/science.1143176.

[18] S. Martelli, E. Perilli, Time-elapsed synchrotron-light microstructural imaging of femoral neck fracture, J. Mech. Behav. Biomed. Mater. 84 (2018) 265–272, doi:10.1016/j.jmbbm.2018.05.016.

[19] B.C.C. Khoo, K. Brown, C. Cann, K. Zhu, S. Henzell, V. Low, S. Gustafsson, R.I. Price, R.L. Prince, Comparison of QCT-derived and DXA-derived areal bone mineral density and T scores, Osteoporos Int 20 (2009) 1539–1545, doi:10.1007/s00198-008-0820-y.

[20] G. Bergmann, G. Deuretzbacher, M. Heller, F. Graichen, A. Rohlmann, J. Strauss, G.N. Duda, Hip contact forces and gait patterns from routine activities, J. Biomech. 34 (2001) 859–871.

[21] E. Dall'Ara, M. Peña-Fernández, M. Palanca, M. Giorgi, L. Cristofolini, G. Tozzi, Precision of digital volume correlation approaches for strain analysis in bone imaged with micro-computed tomography at different dimensional levels, Front. Mater. 4 (2017) 31, doi:10.3389/fmats.2017.00031.

[22] E. Dall'Ara, D. Barber, M. Viceconti, About the inevitable compromise between spatial resolution and accuracy of strain measurement for bone tissue: A 3D zero-strain study, J. Biomech. 47 (2014) 2956–2963, doi:10.1016/j.jbiomech.2014.07.019.

[23] M. Palanca, L. Cristofolini, E. Dall'Ara, M. Curto, F. Innocente, V. Danesi, G. Tozzi, Digital volume correlation can be used to estimate local strains in natural and augmented vertebrae: An organ-level study, J. Biomech. 49 (2016) 3882–3890, doi:10.1016/j.jbiomech.2016.10.018.

[24] J. Schindelin, I. Arganda-carreras, E. Frise, V. Kaynig, M. Longair, T. Pietzsch, S. Preibisch, C. Rueden, S. Saalfeld, B. Schmid, J.Y. Tinevez, D.J. White, V. Hartenstein, K. Eliceiri, P. Tomancak, A. Cardona, Fiji: An open-source platform for biological-image analysis, Nat. Methods. 9 (2012) 676–682, doi:10.1038/nmeth.2019.

[25] T.P. Ruedi, W.M. Murphy, Principles of Fracture Management, Thieme Stuttgart, 2000.

[26] F. Pauwel, Der Schenkenholsbruck em mechanisches problem, Gd. Des Heilungsvorganges Progn. Und Kausale Ther. Stuttgart, Ger. Ferdinand Engke. (1934).

[27] A. Limaye, Drishti: a volume exploration and presentation tool, in: S.R. Stock (Ed.), SPIE Opt. Eng. + Appl., SPIE, 2012, p. 85060X, doi:10.1117/12.935640.

[28] I.R. Reid, No more fracture trials in osteoporosis? Lancet Diabetes Endocrinol 8 (2020) 650–651, doi:10.1016/S2213-8587(20)30232-1.

[29] P. Zioupos, U. Hansen, J.D. Currey, Microcracking damage and the fracture process in relation to strain rate in human cortical bone tensile failure, J. Biomech. 41 (2008) 2932–2939, doi:10.1016/j.jbiomech.2008.07.025.

[30] O. Ariza, S. Gilchrist, R.P.P. Widmer, P. Guy, S.J.J. Ferguson, P.A.A. Cripton, B. Helgason, Comparison of explicit finite element and mechanical simulation of the proximal femur during dynamic drop-tower testing, J. Biomech. 48 (2015) 224–232, doi:10.1016/j.jbiomech.2014.11.042.

[31] B. Helgason, S. Gilchrist, O. Ariza, J.D. Chak, G. Zheng, R.P. Widmer, Development of a balanced experimental – computational approach to understanding the mechanics of proximal femur fractures, Med. Eng. Phys. 36 (2014) 793–799, doi:10.1016/j.medengphy.2014.02.019.

[32] M. Palanca, E. Perilli, S. Martelli, Body anthropometry and bone strength conjointly determine the risk of hip fracture in a sideways fall, Ann. Biomed. Eng. (2020), doi:10.1007/s10439-020-02682-y.

[33] B. Helgason, E. Perilli, E. Schileo, F. Taddei, S. Brynjólfsson, M. Viceconti, Mathematical relationships between bone density and mechanical properties: a literature review, Clin. Biomech. (Bristol, Avon) 23 (2008) 135–146, doi:10.1016/j.clinbiomech.2007.08.024.

[34] C.A. Bailey, K. Brooke-Wavell, Exercise for optimising peak bone mass in women, Proc. Nutr. Soc. 67 (2008) 9–18, doi:10.1017/S0029665108005971.

[35] S. Martelli, B. Beck, D. Saxby, D. Lloyd, P. Pivonka, M. Taylor, Modelling human locomotion to inform exercise prescription for osteoporosis, Curr. Osteoporos. Rep. 18 (2020), doi:10.1007/s11914-020-00592-5.